

Towards synchrotron phase-contrast lung imaging in patients – a proof-of-concept study on porcine lungs in a human-scale chest phantom

Willi L. Wagner,^{a,b} Felix Wuennemann,^{a,b} Serena Pacilé,^{c,d} Jonas Albers,^e Fulvia Arfelli,^f Diego Dreossi,^c Jürgen Biederer,^{a,b} Philip Konietzke,^{a,b} Wolfram Stiller,^{a,b} Mark O. Wielpütz,^{a,b} Agostino Accardo,^d Marco Confalonieri,^g Maria Cova,^h Joachim Lotz,^{e,i} Frauke Alves,^{e,i,k} Hans-Ulrich Kauczor,^{a,b} Giuliana Tromba^c and Christian Dullin^{e,c,j*}

Received 28 March 2018

Accepted 20 September 2018

Edited by A. Momose, Tohoku University, Japan

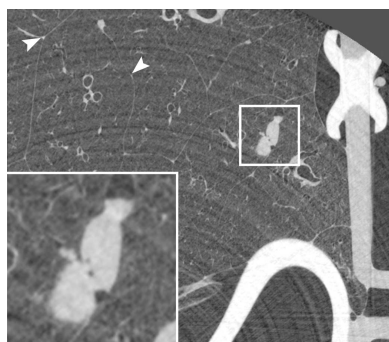
Keywords: propagation based imaging; phase retrieval; synchrotron radiation; preclinical chest phantom; high-resolution porcine lung imaging.

^aDiagnostic and Interventional Radiology, University Hospital Heidelberg, Heidelberg, Germany, ^bTranslational Lung Research Center (TLRC), German Center for Lung Research (DZL), University of Heidelberg, Heidelberg, Germany, ^cElettra-Sincrotrone Trieste, Trieste, Italy, ^dDepartment of Engineering and Architecture, University of Trieste, Trieste, Italy, ^eInstitute for Diagnostic and Interventional Radiology, University Medical Center Goettingen, Goettingen, Germany, ^fDepartment of Physics, University of Trieste and INFN, Trieste, Italy, ^gPulmonology Unit, University Hospital of Cattinara, Trieste, Italy, ^hDepartment of Radiology, University of Trieste, ASUITS, Trieste, Italy, ⁱGerman Center for Cardiovascular Research (DZHK), Partner Site Goettingen, Goettingen, Germany, ^jTranslational Molecular Imaging, Max-Planck-Institute for Experimental Medicine, Goettingen, Germany, and ^kClinic for Haematology and Medical Oncology, University Medical Center Goettingen, Goettingen, Germany. *Correspondence e-mail: christian.dullin@gmail.com

In-line free propagation phase-contrast synchrotron tomography of the lungs has been shown to provide superior image quality compared with attenuation-based computed tomography (CT) in small-animal studies. The present study was performed to prove the applicability on a human-patient scale using a chest phantom with ventilated fresh porcine lungs. Local areas of interest were imaged with a pixel size of 100 μm , yielding a high-resolution depiction of anatomical hallmarks of healthy lungs and artificial lung nodules. Details like fine spiculations into surrounding alveolar spaces were shown on a micrometre scale. Minor differences in artificial lung nodule density were detected by phase retrieval. Since we only applied a fraction of the X-ray dose used for clinical high-resolution CT scans, it is believed that this approach may become applicable to the detailed assessment of focal lung lesions in patients in the future.

1. Introduction

Propagation-based imaging (PBI) has proven to provide images with increased contrast-to-noise ratios (CNRs) at a relatively low dose when compared with classical attenuation-based computed tomography (Fedon *et al.*, 2018), especially for soft-tissue samples (Kitchen *et al.*, 2017). A successful clinical application of PBI for phase-contrast mammography in human patients has been reported (Tromba *et al.*, 2010; Castelli *et al.*, 2011). As a result of their high porosity, deep location and breathing motion, lungs are challenging for most imaging techniques. However, computed tomography (CT) and synchrotron tomography (ST) are well suited for lung imaging because the air in the alveolar spaces and conducting airways offers a high intrinsic contrast compared with the soft-tissue component of the lung. In addition, the strong scattering of the incident X-ray beam within the lung allows the application of phase-sensitive techniques such as PBI and analyzer-based imaging (Kitchen *et al.*, 2004; Dullin, Larsson *et al.*, 2015; Scherer *et al.*, 2017). Several studies demonstrate the benefit of PBI in preclinical animal lung models (Dullin, dal Monego *et*



© 2018 International Union of Crystallography

al., 2015; Gradl *et al.*, 2017). However, two major limitations need to be addressed when discussing a clinical application of synchrotron radiation. Firstly, the vertical beam size is rather limited at synchrotron light sources compared with the size of a human chest. Secondly, ST imaging at a high spatial resolution will still result in high radiation doses, despite the gain in contrast caused by the application of PBI. For these reasons, a clinical application using synchrotron radiation to image the entire human lung currently seems unlikely. However, in some patients the high-resolution assessment of preselected local regions of interest could provide a superior non-invasive diagnosis of patchy structural lung changes as in diffuse parenchymal lung disease (DPLD). DPLD encompasses a large group of lung conditions affecting the pulmonary interstitium, which can be classified by their radiologic pattern (Travis *et al.*, 2013). Idiopathic interstitial fibrosis (IPF), a specific form of DPLD of unknown origin, is characterized radio-pathologically by a usual interstitial pneumonia (UIP) pattern and is associated with a particularly poor clinical outcome (Raghu *et al.*, 2011). Recent micro-CT studies of *ex vivo* tissue cores of explanted IPF-lungs demonstrated the benefits of high-resolution imaging in the assessment of DPLD (Mai *et al.*, 2017). For example, a high-resolution PBI acquisition of a preselected region of interest defined by a routine clinical CT study could potentially help to avoid an invasive lung biopsy in some cases, which is known to be associated with a particularly high risk of complications for patients with suspected IPF (Wiener *et al.*, 2013; Raj *et al.*, 2017). The present pilot study investigated the potential of PBI to perform local-area acquisitions on a human-scale chest phantom prepped with fresh porcine lungs and artificial lung nodules with different concentrations of iodine contrast agent as a model for high-resolution PBI of lung pathology.

2. Methods

2.1. ARTIChest – human-scale chest phantom

A commercially available lung phantom for imaging porcine heart and lung explants (ARTIChest, PROdesign GmbH, Heiligkreuzsteinach, Germany) was used as previously described (Biederer & Heller, 2003). The system is constructed of a copolymer container to simulate a human-scale chest that holds an inflated porcine heart–lung explant by continuous evacuation of the artificial lubricant-prepped pleural space with a pressure of -2 to -3 kPa, simulating near-human physiological conditions. Here, we used fresh porcine lung explants to simulate conditions close to the *in vivo* situation.

2.2. Porcine lungs

Freshly excised heart and lung explants from six mature pigs were analysed paying meticulous attention that the lung surface was intact to prevent air leaks. No animal was sacrificed for the particular purpose of this study. The preparations passed the regular veterinarian controls of a licenced slaughterhouse and were treated with the same hygiene precautions

as fresh meat. Storage, transport, handling and disposal of faunal byproducts were registered at the responsible veterinary office. The image data of two porcine lungs are presented below.

2.3. Preparation of the artificial lung nodules

Artificial lung nodules were induced by injection of 3% agarose gel, containing either 0.5% or 1.0% of a clinical contrast agent with an iodine content of 300 mg ml^{-1} (Accupaque 300, GE Healthcare, Little Chalfont, UK), as previously described (Wielpütz *et al.*, 2015). The concentration of 0.5% Accupaque 300 has been shown to mimic the X-ray attenuation of soft tissue with an average of 80 HU (HU = Hounsfield unit), tested in the same lung as used in the PBI studies (data not shown). The agarose mixture was kept in a water bath at 40°C and directly administered into the inflated lung using a 1 ml syringe and a 28 G cannula. After penetrating the pleura with the needle, approximately 15–20 mixture deposits ranging from 0.025 ml to 0.2 ml were placed into the inflated lung parenchyma of the right lower lobe at variable depths of 1–4 cm (Fig. 2). The needles were removed after a delay of 30 s to allow for hardening of the agarose mixture at room temperature. Around 2–6 artificial lung nodules were created per lung, adding up to total of 22 nodules in six lungs.

2.4. Data acquisition

Local-area acquisitions of the lungs in the ARTIChest phantom were performed at the SYRMEP beamline of the Italian synchrotron light source Elettra with the following parameters: a quasi-monochromatic X-ray beam ($E = 40 \text{ keV}$), a sample-to-detector distance of 2600 mm, a 17.55 mm aluminium filter and $158.0 \text{ mm} \times 3.5 \text{ mm}$ beam dimensions. The customized XCounter Flite FX2 photon-counting detector (Direct Conversion, Danderyd, Sweden) based on CdTe-CMOS with a pixel size of $100 \mu\text{m} \times 100 \mu\text{m}$ was utilized for acquiring 8100 frames, with 45 frames s^{-1} using a low-energy threshold of 19 keV. The rotator was set to a speed of 1° s^{-1} ; therefore, the overall acquisition time was 3 min. The total entrance air kerma measured with a calibrated air ionization chamber during the ST acquisitions was between 10 and 13 mGy.

For comparison, two lungs within ARTIChest have been scanned additionally at the ‘Ospedale di Cattinara’, Trieste, Italy, using an iCT 256 (Philips GmbH, Hamburg, Germany). Scans with different protocols were acquired. In this publication, we used the high-resolution lung CT scans in axial mode, a voxel size of $0.45 \text{ mm} \times 0.45 \text{ mm} \times 0.9 \text{ mm}$, 200 mAs and 120 kVp for comparison.

2.5. Image data post-processing, phase-retrieval and reconstruction

The customized XCounter Flite FX2 detector used in our study consists of 24 separate modules. This design resulted in small gaps of about 100–200 μm in between the modules. Moreover, pixels close to the gap region show a different response to irradiation than in other parts of the detector.

Therefore, the acquired angular projections were processed with custom-made post-processing software. The resulting datasets were then reconstructed using *Syrmep Tomo Project* (STP v1.2.5) (Brun *et al.*, 2015). Prior to reconstruction, the Paganin single-distance phase-retrieval algorithm (Paganin *et al.*, 2002) implemented in the same software was used with a delta-to-beta ratio of 2152 (<https://www.ts-imaging.net/Services/Simple/ICUtilXdata.aspx>).

3. Results and discussion

With this study, we have proven that local-area high-resolution acquisitions can be performed on human-scale inflated porcine lungs with only a fraction of the X-ray dose of clinical state-of-the-art high-resolution lung CT. Thus, we believe our approach could also be feasible for future application in patients. We report on the first application of in-line free propagation phase-contrast CT on a human-scale chest phantom prepped with an inflated fresh porcine lung. The large size of 75 cm × 45 cm × 28 cm and the relatively heavy weight of 11.3 kg (including the lung explant) of the phantom posed challenges for the setup of the SYRMEP beamline. The complete sample stage, including the rotator, was replaced and a dedicated holder fitted to phantom and rotator was manufactured. Fig. 1(a) shows the ARTIChest human chest phantom with an inflated porcine lung (p) mounted on top of the rotational stage (r) using the specially developed vertical phantom holder adaptor. In the background, the beam outlet (b) can be seen. The final setup allowed for a rotation speed of 1° s⁻¹, which will need to be increased in a future setup dedicated for patients. The current total acquisition time for 8100 angular projections is 3 min. We demonstrated in this manuscript that reconstructions based on only a third of the

projections did not display any strong differences in quality, which would already reduce the total acquisition time to 1 min. In addition, from the application of PBI for breast CT on human mastectomy samples we evaluated that an increased sample-to-detector distance of approximately 9 m further increases the efficiency of PBI by approximately a factor of three using the same detector with a pixel size of 100 μm (Baran *et al.*, 2017). We plan to exploit this for a follow-up experiment with the human chest phantom, allowing a further reduction in the acquisition time by a factor of three. Moreover, due to the fact that the dose used in this pilot study was significantly lower than for a clinical CT acquisition, the image acquisition could be speeded up by using a slightly higher dose while still maintaining the demonstrated image quality. Therefore, we believe we could reduce the total acquisition time in further experiments to below 10 s, which will be a pivotal aspect to pave the way for a single breath-hold acquisition. At the same time, the rotation speed must be adjusted to values tolerable by patients. We plan to implement a rotating chair for the patients. For an acquisition of 10 s the angular speed would therefore be 18° s⁻¹ which we believe is tolerable even for sick patients because the rotation axis is in the middle of the patient.

However, in this proof-of-concept study the lungs were imaged in a steady state without simulating breathing motion. A continuous breath-hold manoeuvre by application of negative pressure to the artificial pleural space allowed for a physiological passive inflation of the fresh porcine lungs. We demonstrated the feasibility of imaging local areas of interest of 140 mm × 140 mm × 4 mm at a spatial resolution of 100 μm, compared with 400–600 μm obtained in commonly used clinical CTs. The high-resolution acquisition allows for a very detailed assessment of the anatomical hallmarks

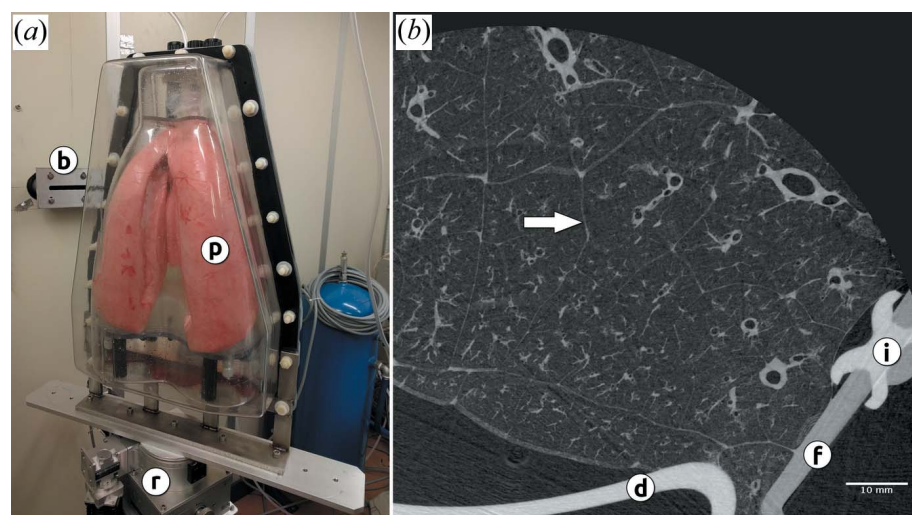


Figure 1

(a) The chest phantom (p) with an inflated porcine lung mounted on top of the rotational stage (r) in front of the beam outlet (b). (b) Maximum intensity projection of five consecutive slices of a reconstructed local area acquisition on the periphery of the right lower lung lobe (after phase retrieval) is shown. The phase contrast allows a detailed depiction of airways, pulmonary blood vessels and interlobular septa (white arrow). (f) indicates the front cover of the phantom, (d) marks the artificial diaphragm and (i) depicts a silicon injection port. Scale bar in (b) = 10 mm.

in ventilated healthy porcine lung as illustrated for one specimen with a maximum intensity projection over five consecutive slices (Fig. 1b). Individual interlobular septa (white arrow in Fig. 1b) can be clearly delineated by a fine smooth linear density in the lung parenchyma, which is not the case in pigs as well as in the human lung. The fact that the interlobular septum can already be depicted in great detail in healthy lungs is an important finding, as it is a key anatomical landmark in the pathophysiology and radiological assessment of many pulmonary diseases. The interlobular septum defines the pulmonary lobule as the smallest lung structure delimited by connective tissue septa (Webb, 2006; Miller, 1937). The pattern of involvement of the interlobular septa and the pulmonary lobule differs characteristically in several interstitial lung diseases and contributes to their radiological classification

(Webb, 2006). With respect to the pulmonary lobule as an anatomical unit, recent studies demonstrated the benefit of high-resolution assessment of preselected local areas of interest by providing new insights into the spatio-temporal progress of structural changes in idiopathic pulmonary fibrosis by micro-CT studies of human tissue cores (Mai *et al.*, 2017). In our study, we intend to advance into the same direction of high-resolution assessment of preselected local areas of interest, although in a setting closer to future clinical applications.

The ARTIChest phantom also features an outer cover with silicon sealed injection ports [(i) in Fig. 1*b*], through which artificial lung nodules were generated by injecting 3% low-melting-point agarose, supplemented with two different concentrations of iodine-based contrast medium, to mimic lung nodules with densities close to human soft-tissue masses. Fig. 2(*a*) shows close-up images of the lung parenchyma of a second lung adjacent to the injection port after injection of two artificial lung nodules. Subsequently, the same region was imaged at an even lower entrance dose of 13 mGy air kerma. The results of the reconstruction are shown in Fig. 2(*a*) without phase retrieval (RAW), after application of phase retrieval (PHR) and using only one-third of the acquired projections (PHR 1/3), thereby lowering the entrance dose required for the acquisition down to ~ 4 mGy.

PBI not only allowed for a strong reduction in X-ray dose but also for the detection of fine spiculations of the artificial lung nodules that were caused by the agarose gel entering the surrounding alveolar spaces, which was not possible to visualize in clinical CT. We measured a contrast-to-noise ratio of 0.7 (RAW), 7 (PHR) and 7 (PHR 1/3) between the lung nodule and the surrounding tissue. Since the regions used for this estimation were not completely homogeneous, the calculated noise is most likely an overestimation of the real situation. The reported CNR values are therefore underestimated. However, we found an about tenfold increase in CNR after phase retrieval. This is in accordance with results that we obtained in mice lungs (Mohammadi *et al.*, 2014). Moreover, we found no significant difference between PHR and PHR 1/3, thereby verifying that one-third of the acquired project are still sufficient for the reconstruction. As a result of the increased CNR the PHR image allows for the best evaluation of lung structure and nodules. Moreover, the RAW image data without phase retrieval did not depict the slight difference in density between the two nodules (blue line in Fig. 2*b*). Only after phase retrieval were the different densities detectable (orange line in Fig. 2*b*). The subtle variations in the profile plot of the RAW data (Fig. 2*b*) originate most likely from imaging artefacts (stripes visible in Fig. 2*a*), phase effects and noise, but it cannot be excluded that they also partially present the

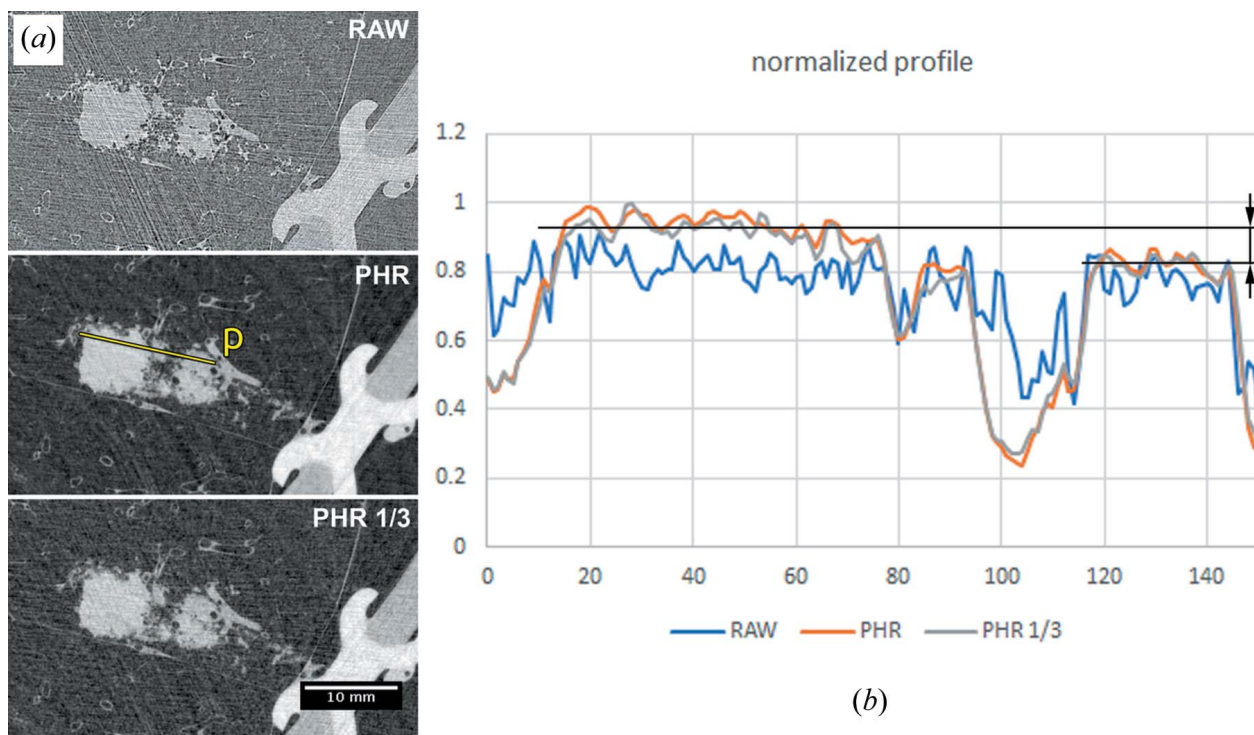


Figure 2
 (*a*) Detailed views of two artificial lung nodules acquired at an entrance dose of ~ 13 mGy air kerma and reconstructed without phase retrieval (RAW), with phase retrieval (PHR) and with a subset of a third of the angular projections. PHR demonstrates the best image quality, showing minute air enclosures within the nodule and fine spiculations protruding into the surrounding alveoli. (*b*) Profile plots at the line indicated in yellow (normalized to a maximum of 1). Without phase retrieval no density difference between the nodules can be detected (RAW). Phase retrieval (PHR) allowed for differentiation of nodule densities. Note that a reduction in used projections (PHR 1/3) did not impair the sensitivity in density differentiation. [Images are displayed with auto-scaled grey values (minimum = black, maximum = white) explaining the differences in the appearance of the data.]

substructure of the analysed region. The applied TIE-Hom method will not only remove the phase effects but its known low-pass filtering effects might suppress these features. However, we believe that the gain in CNR is more beneficial for diagnosis and automated image analysis. In addition, the dose reduction that can be achieved in PBI compared with classical absorption-based CT allows for acquisitions with higher spatial resolution than possible with the same dose level in clinical systems. Thus, even if subtle details would be suppressed by the low-pass filtering characteristic of the TIE-Hom method, those features would otherwise not have been seen in absorption-based CT.

Interestingly, the sensitivity for the detection of minor density differences was not impaired when the number of used projections was reduced by a third. This suggests that the already very low X-ray dose used for this acquisition could be further reduced.

In order to evaluate the gain in image quality in our PBI application, two specimens have been scanned with a clinical CT scanner (Philips iCT 256) after PBI imaging using different standard clinical CT protocols. In Fig. 3, a comparison of a standard high-resolution lung CT protocol (voxel size $0.45 \text{ mm} \times 0.45 \text{ mm} \times 0.9 \text{ mm}$) (Fig. 3*a*) with our PBI image (voxel size $0.1 \text{ mm} \times 0.1 \text{ mm} \times 0.1 \text{ mm}$) reconstructed with a third of the acquired projections (Fig. 3*b*) is shown. Clearly interlobular septa, margins of bronchi and blood pulmonary vessels as well as the artificial nodule are depicted in greater detail using PBI. Given the strong difference in the voxel sizes, this result is not surprising and must be related to the applied radiation dose. Comparison of clinical dose measurements and dose definitions with measurements at SYRMEP are challenging. Therefore, the following values can only estimate the dose reduction of PBI in our application. For comparison, we measured the 33 mGy air kerma in the clinical scanner using the same acquisition protocol that was applied for the

specimen. Compared with $\sim 13 \text{ mGy}$ in our PBI acquisitions (or $\sim 4 \text{ mGy}$ with a third of the projections) we achieved a dose reduction by 60 or 88%, respectively. Current developments in clinical CT (ultra-high-resolution CT) also show that in these absorption-contrast-based systems a voxel size and resolution of about $0.156 \text{ mm} \times 0.156 \text{ mm} \times 0.250 \text{ mm}$ can be reached using a dose index volume of 19.2 mGy (Hata *et al.*, 2018). While again the dose value can only hardly be related to our results and no CNR are reported, the voxel volume is still six times larger than in our application.

4. Conclusions

In this proof-of-concept study we demonstrate that synchrotron-based local-area free propagation phase-contrast CT can be performed on a human-scale chest phantom prepped with fresh porcine lungs. Moreover, we demonstrated that improved image quality by PBI allows for a more detailed characterization of anatomical landmarks of healthy lungs and the assessment of artificial lung nodules. The applied X-ray dose of $\sim 13 \text{ mGy}$ (air kerma entrance dose) would already allow for a potential translation into clinical application from a radiation exposure point of view and can even be reduced further in future optimized setups. We are aware that a major limitation in the present study is the limited beam size of 4 mm in the z -direction. In a clinical setup, localizing a lung nodule would be practically impossible. If performed using a beam expander or moving the experiment to a different synchrotron facility, this would allow for an increase in the vertical beam size up to a few centimetres. However, the use of phase-contrast CT for virtual local lung biopsies will require a two-step approach: (i) a routine clinical CT of the entire chest to localize sites of interest, followed by (ii) a high-resolution phase-contrast virtual biopsy. Therefore, despite the limitation of our approach, we believe that the presented results pave

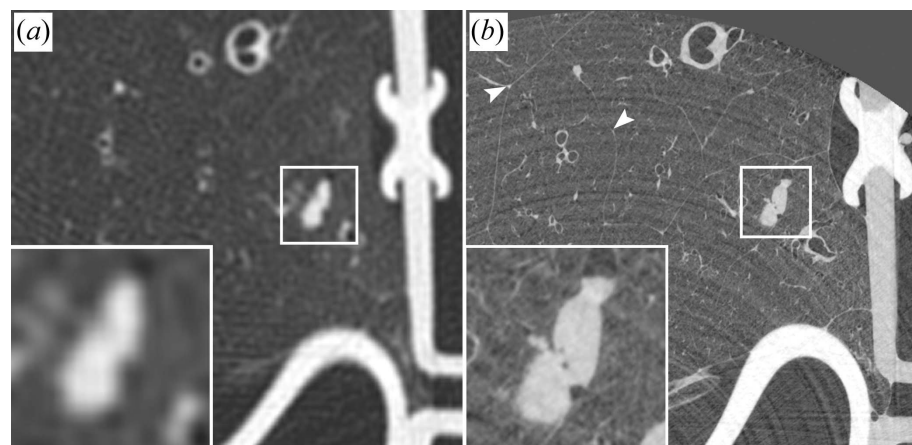


Figure 3

Comparison of a clinical high-resolution lung CT scan (*a*) with a local PBI scan (*b*) on the same specimen including an artificial lung nodule (detailed view). The clinical scan was acquired with a voxel size of $0.45 \text{ mm} \times 0.45 \text{ mm} \times 0.9 \text{ mm}$ (33 mGy air kerma) compared with a voxel size of $0.1 \text{ mm} \times 0.1 \text{ mm} \times 0.1 \text{ mm}$ in PBI (4.3 mGy air kerma, one-third of the projection data used for reconstruction). Clearly the lung structures, including interlobular septa (white arrow heads), margins of subsegmental bronchi and pulmonary blood vessels as well as the nodule are depicted in more detail in (*b*).

the way towards a clinical application in the assessment of preselected local areas of interest. Aside from feasibility, further research is warranted to evaluate how far these high-resolution images might serve as a substitute for lung biopsies, avoiding invasive procedures with associated risks for the patient in a certain subset of clinical cases such as DPLD with possible UIP pattern. The ability to access three-dimensional local lung structure in great detail and without deformations caused by biopsy will complement histopathological evaluation of lung disease. Since the current setup still requires a total acquisition time of 3 min, due to limitations of the rotational unit in combination with the heavy weight of the phantom, further development of the setup is needed to lower acquisition time for clinical use. With respect to

such future potential clinical applications, as a next step, further development is warranted to control the influence of respiratory motion on image quality.

Acknowledgements

The authors thank all people that have been involved in this complex experiment. From the German Center for Cancer Research we thank Dr Philipp Mann and Dr Oliver Sedlacek for their help with the chest phantom, as well as Armin Runz for help with the agarose preparation. Nicola Sodini and Eugenio Nicolini from the technical staff of the Italian synchrotron light source, who did an outstanding job in manufacturing and implementing a novel sample stage, rotator and sample holder for this experiment.

References

Baran, P., Pacile, S., Nesterets, Y. I., Mayo, S. C., Dullin, C., Dreossi, D., Arfelli, F., Thompson, D., Lockie, D. M., McCormack, M., Taba, S. T., Brun, F., Pinamonti, M., Nickson, C., Hall, C., Dimmock, M., Zanconati, F., Cholewa, M., Quiney, H., Brennan, P. C., Tromba, G. & Gureyev, T. E. (2017). *Phys. Med. Biol.* **62**, 2315–2332.

Biederer, J. & Heller, M. (2003). *Radiology*, **226**, 250–255.

Brun, F., Pacilè, S., Accardo, A., Kourousias, G., Dreossi, D., Mancini, L., Tromba, G. & Pugliese, R. (2015). *Fundamenta Informaticae*, **141**, 233–243.

Castelli, E., Tonutti, M., Arfelli, F., Longo, R., Quaia, E., Rigon, L., Sanabor, D., Zanconati, F., Dreossi, D., Abrami, A., Quai, E., Bregant, P., Casarin, K., Chenda, V., Menk, R. H., Rokvic, T., Vascotto, A., Tromba, G. & Cova, M. A. (2011). *Radiology*, **259**, 684–694.

Dullin, C., dal Monego, S., Larsson, E., Mohammadi, S., Krenkel, M., Garrovo, C., Biffi, S., Lorenzon, A., Markus, A., Napp, J., Salditt, T., Accardo, A., Alves, F. & Tromba, G. (2015). *J. Synchrotron Rad.* **22**, 143–155.

Dullin, C., Larsson, E., Tromba, G., Markus, A. M. & Alves, F. (2015). *J. Synchrotron Rad.* **22**, 1106–1111.

Fedon, C., Rigon, L., Arfelli, F., Dreossi, D., Quai, E., Tonutti, M., Tromba, G., Cova, M. A. & Longo, R. (2018). *J. Med. Imaging*, **5**, 013503.

Gratl, R., Dierolf, M., Hehn, L., Günther, B., Yildirim, A. Ö., Gleich, B., Achterhold, K., Pfeiffer, F. & Morgan, K. S. (2017). *Sci. Rep.* **7**, 4908.

Hata, A., Yanagawa, M., Honda, O., Kikuchi, N., Miyata, T., Tsukagoshi, S., Uranishi, A. & Tomiyama, N. (2018). *Acad. Radiol.* **25**, 869–876.

Kitchen, M. J., Buckley, G. A., Gureyev, T. E., Wallace, M. J., Andres-Thio, N., Uesugi, K., Yagi, N. & Hooper, S. B. (2017). *Sci. Rep.* **7**, 15953.

Kitchen, M. J., Paganin, D., Lewis, R. A., Yagi, N., Uesugi, K. & Mudie, S. T. (2004). *Phys. Med. Biol.* **49**, 4335–4348.

Mai, C., Verleden, S. E., McDonough, J. E., Willems, S., De Wever, W., Coolen, J., Dubbeldam, A., Van Raemdonck, D. E., Verbeken, E. K., Verleden, G. M., Hogg, J. C., Vanaudenaerde, B. M., Wuyts, W. A. & Verschakelen, J. A. (2017). *Radiology*, **283**, 252–263.

Miller, W. S. (1937). *Respir. Med.* **31**, 310.

Mohammadi, S., Larsson, E., Alves, F., Dal Monego, S., Biffi, S., Garrovo, C., Lorenzon, A., Tromba, G. & Dullin, C. (2014). *J. Synchrotron Rad.* **21**, 784–789.

Paganin, D., Mayo, S. C., Gureyev, T. E., Miller, P. R. & Wilkins, S. W. (2002). *J. Microsc.* **206**, 33–40.

Raghu, G., Collard, H. R., Egan, J. J., Martinez, F. J., Behr, J., Brown, K. K., Colby, T. V., Cordier, J.-F., Flaherty, K. R., Lasky, J. A., Lynch, D. A., Ryu, J. H., Swigris, J. J., Wells, A. U., Ancochea, J., Bouros, D., Carvalho, C., Costabel, U., Ebina, M., Hansell, D. M., Johkoh, T., Kim, D. S., King, T. E., Kondoh, Y., Myers, J., Müller, N. L., Nicholson, A. G., Richeldi, L., Selman, M., Dudden, R. F., Griss, B. S., Protzko, S. L., Schünemann, H. J. & ATS/ERS/JRS/ALAT Committee on Idiopathic Pulmonary Fibrosis (2011). *Am. J. Respir. Crit. Care Med.* **183**, 788–824.

Raj, R., Raparia, K., Lynch, D. A. & Brown, K. K. (2017). *Chest*, **151**, 1131–1140.

Scherer, K., Yaroshenko, A., Bölükbas, D. A., Gromann, L. B., Hellbach, K., Meinel, F. G., Braunagel, M., von Berg, J., Eickelberg, O., Reiser, M. F., Pfeiffer, F., Meiners, S. & Herzen, J. (2017). *Sci. Rep.* **7**, 402.

Travis, W. D., Costabel, U., Hansell, D. M., King, T. E., Lynch, D. A., Nicholson, A. G., Ryerson, C. J., Ryu, J. H., Selman, M., Wells, A. U., Behr, J., Bouros, D., Brown, K. K., Colby, T. V., Collard, H. R., Cordeiro, C. R., Cottin, V., Crestani, B., Drent, M., Dudden, R. F., Egan, J., Flaherty, K., Hogaboam, C., Inoue, Y., Johkoh, T., Kim, D. S., Kitaichi, M., Loyd, J., Martinez, F. J., Myers, J., Protzko, S., Raghu, G., Richeldi, L., Sverzellati, N., Swigris, J., Valeyre, D. & ATS/ERS Committee on Idiopathic Interstitial Pneumonias (2013). *Am. J. Respir. Crit. Care Med.* **188**, 733–748.

Tromba, G., Longo, R., Abrami, A., Arfelli, F., Astolfo, A., Bregant, P., Brun, F., Casarin, K., Chenda, V. & Dreossi, D. (2010). *AIP Conf. Proc.* **1266**, 18–23.

Webb, W. R. (2006). *Radiology*, **239**, 322–338.

Wielpütz, M. O., Wroblewski, J., Lederlin, M., Dinkel, J., Eichinger, M., Koenigkam-Santos, M., Biederer, J., Kauczor, H.-U., Puderbach, M. U. & Jobst, B. J. (2015). *Eur. J. Radiol.* **84**, 1005–1011.

Wiener, R. S., Wiener, D. C. & Gould, M. K. (2013). *Clin. Pulm. Med.* **20**, 29–35.